

## Article

# An Ice-Penetrating Signal Denoising Method Based on WOA-VMD-BD

Danping Lu <sup>1,2,3</sup> , Shaoxiang Shen <sup>1,2,\*</sup>, Yuxi Li <sup>1,2</sup>, Bo Zhao <sup>1,2</sup>, Xiaojun Liu <sup>1,2</sup> and Guangyou Fang <sup>1,2,3,\*</sup><sup>1</sup> Aerospace Information Research Institute, Chinese Academy of Sciences, Beijing 100094, China<sup>2</sup> Key Laboratory of Electromagnetic Radiation and Sensing Technology, Chinese Academy of Sciences, Beijing 100190, China<sup>3</sup> School of Electronic, Electrical and Communication Engineering, University of Chinese Academy of Sciences, Beijing 100049, China

\* Correspondence: sxshen@mail.ie.ac.cn (S.S.); gyfang@mail.ie.ac.cn (G.F.)

**Abstract:** Chang'E-7 will be launched around 2026 to explore resources at the lunar south pole. Glaciers are suitable scenes on the earth for lunar penetrating radar verification. In the verification experiment, ice-penetrating signals are inevitably polluted by noise, affecting the accuracy and reliability of glacier detection. This paper proposes a denoising method for ice-penetrating signals based on the combination of whale optimization algorithm (WOA), variational mode decomposition (VMD), and the improved Bhattacharyya distance (BD). Firstly, a fitness function for WOA is established based on permutation entropy (PE), and the number of decomposition modes  $K$  and the quadratic penalty factor  $\alpha$  in the VMD are optimized using WOA. Then, VMD is performed on the signal to obtain multiple intrinsic mode functions (IMFs). Finally, according to the BD, the relevant IMFs are selected for signal reconstruction and denoising. The simulation results indicate the strengths of this method in enhancing the signal-to-noise ratio (SNR), and its performance is better than empirical mode decomposition (EMD). Experiments on the detected signals of the Mengke Glacier No. 29 indicate that the WOA-VMD-BD method can efficiently eliminate noise from the data and procure well-defined layered profiles of the glacier. The research in this paper helps observe the layered details of the lunar regolith profile and interpret the data in subsequent space exploration missions.

**Keywords:** ice-penetrating signal; VMD; WOA; BD; parameter optimization; IMFs; denoising**Citation:** Lu, D.; Shen, S.; Li, Y.; Zhao, B.; Liu, X.; Fang, G. An

Ice-Penetrating Signal Denoising Method Based on WOA-VMD-BD.

*Electronics* **2023**, *12*, 1658. <https://doi.org/10.3390/electronics12071658>

Academic Editors: Ning Li and Koo Voon Chet

Received: 24 February 2023

Revised: 28 March 2023

Accepted: 29 March 2023

Published: 31 March 2023



**Copyright:** © 2023 by the authors. Licensee MDPI, Basel, Switzerland. This article is an open access article distributed under the terms and conditions of the Creative Commons Attribution (CC BY) license (<https://creativecommons.org/licenses/by/4.0/>).

## 1. Introduction

In 2004, China officially launched the lunar exploration project, named the “Chang’e Project”. Previously, China’s lunar exploration program was planned in three phases: orbiting, landing, and returning. “Orbiting” referred to the lunar orbit exploration carried out from 2004 to 2007; “landing” referred to the first soft landing on the moon and automatic reconnaissance and surveying around 2013; “returning” referred to the first automated sampling and returning of lunar samples before 2020. The fourth phase of the lunar exploration project, Chang’E-7, is expected to be launched around 2026 and will land on the moon’s south pole to carry out resource exploration. The landing site is located in the Antarctic–Aitken Basin region above 85 degrees south latitude on the moon. As one of the vital payloads deployed in the Chang’E-7 mission, the lunar-penetrating radar utilizes both single-polarization and multi-polarization modes for detecting the thickness and exposing the layered structure of the lunar regolith, providing a scientific basis for the study of the shallow structure of the moon. The relative permittivity of lunar regolith is approximately between 3–4, similar to the relative permittivity of glaciers on the earth. Therefore, glaciers with high altitude, low pressure, and low temperature are suitable scenes for lunar-penetrating radar verification.

Pseudo-random coded ultra-wideband (UWB) radar has the advantages of a high signal-to-noise ratio (SNR) and high range resolution [1], which provides technical support

for detecting shallow structures of the moon. However, the signals acquired by pseudo-random coded UWB radar are still inevitably polluted by various noise sources, including environmental noise and human interference. This leads to inaccurate results and hinders the interpretation of the acquired data.

The denoising of ice-penetrating signals is an essential aspect of improving the accuracy and reliability of ice detection. The development of radar signal denoising technology has become increasingly mature, including Fourier transform [2],  $f - k$  filtering [3], wavelet transform [4], and other methods. However, these methods are mainly aimed at stationary signals and are not adaptive, which will limit the processing of non-stationary signals [5,6]. For example, the Fourier transform filter may lose the effective signal with the same frequency as the noise. The apparent velocity parameter of the  $f - k$  filter is difficult to set, and the signal may be distorted. The basis function and decomposition level of the wavelet transform affect the method's performance and may lose the original time domain characteristics.

Therefore, Empirical Mode Decomposition (EMD) is introduced. EMD is a method pioneered by Huang et al. [7], representing non-stationary signals as the sum of intrinsic mode functions (IMFs) with zero means. The signal is represented as a sum of signal-dependent basis functions through a recursive sifting iterative procedure in EMD [8]. However, this method lacks the theoretical basis of mathematical physics and is prone to the aliasing of modal components [9,10]. Variational Mode Decomposition (VMD) is a fully non-recursive variational mode decomposition model proposed by Dragomiretskiy et al., 2014 [11]. VMD can surmount the limitations of EMD and has been widely used in signal denoising [12–18]. In 2019, Cheng et al. applied VMD to denoise the ice-penetrating signals [19]. The practical implementation of this method demonstrates its capability in enhancing the SNR of ice-penetrating radar data.

The VMD decomposition results are significantly impacted by choice of decomposition mode numbers  $K$  and quadratic penalty factor  $\alpha$ , degrading signal denoising performance. It is time-consuming to adjust the parameters manually [20]. Optimizing the parameter combination  $[K, \alpha]$  through the whale optimization algorithm (WOA) can solve the problem of difficult parameter selection. The whale optimization algorithm was proposed by Mirjalili et al., in 2016 [21]. This study proposes a method based on WOA and VMD to decompose the ice-penetrating signals. Use WOA to iteratively calculate the optimal parameters of  $[K, \alpha]$  to VMD, and select some IMFs to reconstruct the signal by calculating the improved Bhattacharyya distance (BD). BD is utilized to quantify the degree of similarity between two probability density functions. Lu et al. proposed an improved BD calculation method using variance instead of the probability density function [22]. The WOA-VMD-BD method can effectively remove the noise in the signal by using the search ability of WOA and the mode decomposition ability of VMD.

The rest of this paper is arranged as follows: Section 2 introduces the principles of VMD briefly. Section 3 illustrates the theory of WOA and the procedure for the WOA-VMD-BD method. Section 4 describes the processing results of the mixed signal and multi-polarization forward modeling signals and compares the denoising capability of the WOA-VMD-BD method and EMD method. Section 5 presents the results of processing the measured glacier data. Section 6 draws general conclusions.

## 2. Brief Description of VMD Theory

VMD can decompose the input signal into  $K$  intrinsic mode functions (IMF) with varying center frequencies and bandwidths [23,24]. VMD can be regarded as a process of solving the optimal solution of the constrained variational problem [25]. The IMF is defined as:

$$u_k(t) = A_k(t) \cos(\phi_k(t)). \quad (1)$$

Here,  $u_k(t)$  is the IMF,  $A_k(t)$  is the instantaneous amplitude,  $\phi_k(t)$  is the phase, and  $t$  represents the time script.

In decomposing the original signal, VMD iteratively updates the center frequency and the bandwidth of each intrinsic mode function. It then performs adaptive frequency band segmentation to obtain several narrowband IMFs based on the frequency characteristics. The IMFs components are compactly centered on their respective center frequencies [26]. The calculated constrained variational problem is:

$$\min_{\{u_k\}, \{\omega_k\}} \left\{ \sum_k \left\| \partial_t \left[ \left( \delta(t) + \frac{j}{\pi t} \right) * u_k(t) \right] e^{-j\omega_k t} \right\|_2^2 \right\} \tag{2}$$

s.t.  $\sum_k u_k = f.$

Here,  $\{u_k\} = \{u_1, \dots, u_K\}$  and  $\{\omega_k\} = \{\omega_1, \dots, \omega_K\}$  are  $K$  IMFs and their center frequencies.  $\|\dots\|_2$  is the norm.  $\partial_t$  is the gradient with respect to  $t$ ,  $\delta(t)$  is the impulse function.  $f$  is the signal to be decomposed.

The quadratic penalty factor  $\alpha$  and the Lagrange multiplier  $\lambda$  are introduced to solve the optimal solution of Equation (2). The augmented Lagrange function is defined as:

$$L(\{u_k\}, \{\omega_k\}, \lambda) = \alpha \sum_k \left\| \partial_t \left[ \left( \delta(t) + \frac{j}{\pi t} \right) * u_k(t) \right] e^{-j\omega_k t} \right\|_2^2 + \left\| f(t) - \sum_k u_k(t) \right\|_2^2 + \left\langle \lambda(t), f(t) - \sum_k u_k(t) \right\rangle. \tag{3}$$

Making use of the Parseval/Plancherel Fourier isometry under the  $L^2$  norm, this problem can be solved in the spectral domain. The iteration formula is expressed as:

$$\hat{u}_k^{n+1}(\omega) = \frac{\hat{f}(\omega) - \sum_{i \neq k} \hat{u}_i^n(\omega) + \frac{\hat{\lambda}^n(\omega)}{2}}{1 + 2\alpha(\omega - \omega_k^n)^2}, \tag{4}$$

$$\omega_k^{n+1} = \frac{\int_0^\infty \omega |\hat{u}_k^n(\omega)|^2 d\omega}{\int_0^\infty |\hat{u}_k^n(\omega)|^2 d\omega}, \tag{5}$$

$$\hat{\lambda}^{n+1}(\omega) = \hat{\lambda}^n(\omega) + \tau \left( \hat{f}(\omega) - \sum_k \hat{u}_k^{n+1}(\omega) \right), \tag{6}$$

where  $\tau$  is the noise tolerance,  $n$  is the iteration number. The iteration termination condition of  $u_k$  is as follows:

$$\sum_k \left\| \hat{u}_k^{n+1} - \hat{u}_k^n \right\|_2^2 / \left\| \hat{u}_k^n \right\|_2^2 < \varepsilon, \tag{7}$$

where  $\varepsilon$  represents tolerance of convergence criterion, which is typically around  $10^{-6}$ .

### 3. Principle of the WOA-VMD-BD Model

#### 3.1. Whale Optimization Algorithm

When humpback whales are hunting, they dive under the prey and generate dense air bubbles during the upward spiral process, forcing the prey to be surrounded by the ring formed by the air bubble net. Inspired by the predation behavior, the whale optimization algorithm (WOA) was proposed by Mirjalili et al., in 2016 [21]. The algorithm exhibits several advantages, including fewer input parameters, high convergence accuracy, solid global search capability, and strong robustness [27].

The WOA consists of three processes: encircling prey, spiral bubble-net predation, and randomly searching for prey. In order to complete the simulation optimization, the math model of each process is expressed as follows:

- (1) Encircling prey

During hunting, humpback whales can detect the location of the prey and encircle them. However, obtaining the optimal global solution in the initial state is not feasible. Therefore, it is assumed that the initial position of the target prey or a position close to the prey represents the current optimal whale position [26]. Once the optimal whale position is determined, the remaining whales update their positions continuously, which can be expressed using the following equation:

$$\vec{D} = \left| \vec{C} \cdot \vec{X}_i^* - \vec{X}_i \right|, \tag{8}$$

$$\vec{X}_{i+1} = \vec{X}_i^* - \vec{A} \cdot \vec{D}, \tag{9}$$

$$\vec{A} = 2\vec{a} \cdot \vec{r} - \vec{a}, \tag{10}$$

$$\vec{C} = 2 \cdot \vec{r}. \tag{11}$$

Here,  $\vec{X}^*$  represents the optimal whale position vector, given randomly for the first time. The current position vector of the whale is represented by  $\vec{X}$ .  $\vec{D}$  represents the search distance. Both  $\vec{A}$  and  $\vec{C}$  are coefficient vectors. In the iterative search process,  $\vec{a}$  decreases linearly in  $[2, 0]$ , and  $\vec{r} \in [0, 1]$  is a random vector.  $i$  is the current number of iterations.

(2) Spiral bubble-net predation

During the spiral bubble net attack, WOA uses two predation strategies: shrinking encircling and spiral update position.

The WOA incorporates a random strategy selection probability,  $p \in [0, 1]$  to simulate these two strategies. When the probability  $p < 0.5$ , the whale adopts a shrinking encircling strategy. When the probability  $p \geq 0.5$ , the whale adopts the spiral update position strategy. First, the distance between the whale and its prey was calculated. Next, a spiral equation was established between the whale’s position and that of its prey:

$$\vec{X}_{i+1} = \vec{D}' \cdot e^{bl} \cdot \cos(2\pi l) + \vec{X}_i^*, \tag{12}$$

where  $\vec{D}' = \left| \vec{X}_i^* - \vec{X}_i \right|$  represents the distance between the current whale and the prey.  $b$  is a constant of logarithmic spiral shape.  $l \in [0, 1]$  is a random number.

The probability of both behaviors is 50%. The mathematical model is given as follows:

$$\vec{X}_{i+1} = \begin{cases} \vec{X}_i^* - \vec{A} \cdot \vec{D} & p < 0.5 \\ \vec{D}' \cdot e^{bl} \cdot \cos(2\pi l) + \vec{X}_i^* & p \geq 0.5. \end{cases} \tag{13}$$

(3) Random search for prey

To enhance the search capability of the WOA, whales engage in random prey searching. If  $A \geq 1$ , the whale chooses to search for prey randomly and updates the position according to the random whale position:

$$\vec{D} = \left| \vec{C} \cdot \vec{X}_{\text{rand}} - \vec{X} \right|, \tag{14}$$

$$\vec{X}_{i+1} = \vec{X}_{\text{rand}} - \vec{A} \cdot \vec{D}, \tag{15}$$

where  $\vec{X}_{\text{rand}}$  represents the position vector of a randomly selected whale from the whale population.

3.2. Improved VMD Based on WOA

Selecting different parameter combinations  $[K, \alpha]$  for VMD based solely on empirical values can lead to significant randomness and errors, resulting in issues such as spectral aliasing and unstable bandwidths. Furthermore, manual adjustment of parameters is often

time-consuming. Therefore, it is essential to set critical parameters reasonably in the VMD. We used WOA to optimize the two parameters,  $K$  and  $\alpha$ .

When WOA is used to optimize the parameters of VMD, the selection of the fitness function of the WOA will affect the optimal results of  $K$  and  $\alpha$ , thus affecting the performance of the WOA-VMD-BD method. Permutation entropy (PE) can amplify the weak time series changes. Its characteristics, such as fast calculation speed and strong noise-robustness, make it well-suited for analyzing signals containing dynamic noise. In this paper, the fitness function is constructed based on permutation entropy [28]. We give the calculation process of permutation entropy.

Given a series  $\{x(1), x(2), \dots, x(N)\}$ , set embedding dimension  $m$  and time delay  $L$ . The sequence is reconstructed to obtain the following reconstruction matrix:

$$Y = \begin{pmatrix} x(1) & \cdots & x(1 + (m - 1)t) \\ \vdots & \ddots & \vdots \\ x(K) & \cdots & x(r + (m - 1)t), \end{pmatrix} \tag{16}$$

where  $r$  is the number of reconstructed row vectors,  $r = N - (m - 1)L$ . The row vectors in the reconstruction matrix are arranged in ascending order of element values, where the  $j$ th row is expressed as:

$$x(j + (q_{j1} - 1)t) \leq x(j + (q_{j2} - 1)t) \leq \cdots \leq x(j + (q_{jm} - 1)t), j \in [1, r], \tag{17}$$

where  $r \leq m!$ ,  $m!$  is the total number of symbol sequences mapped in  $m$ -dimensional phase space. According to the index of the position of each element, the symbol sequence  $S(j) = \{q_{j1}, q_{j2}, \dots, q_{jm}\}$  of each row is obtained. The probability of occurrence of  $r$  different symbol  $S(j)$  is  $P_1, P_2, \dots, P_r$ , respectively. The PE of  $\{x(1), x(2), \dots, x(N)\}$  is denoted by:

$$H_{pe} = - \sum_{j=1}^r P_j \ln P_j. \tag{18}$$

The PE value of IMFs obtained by the WOA-VMD-BD method will change with the set parameters  $[K, \alpha]$ . During the execution process iterations, the variance increases substantially as the PE values of  $K$  IMFs exhibit significant fluctuations. Conversely, each iteration's mean of  $K$  PE values undergoes minimal changes. When the ratio of mean to variance is small, it leads to the accurate separation of the target signal's IMFs and noisy IMFs. When the ratio of mean to variance is small, accurate separation of the IMFs of the target signal and the IMFs of the noise signal is achieved. The fitness function to obtain the optimal solution for the parameter  $[K, \alpha]$  utilizes the mean-to-variance ratio of PE as the fitness function. It employs the minimum value of the fitness function as the search target for the WOA. The fitness function can be expressed as:

$$fitness = \frac{\text{mean}(H_{pe}(IMF_k))}{\text{var}(H_{pe}(IMF_k))}. \tag{19}$$

### 3.3. Selection of Relevant IMFs

The Bhattacharyya distance (BD) can be applied to select relevant IMFs in VMD. This method utilizes an improved BD measure to evaluate the similarity between the variances, thereby distinguishing relevant IMF components from irrelevant ones.

Assume  $X$  is the input signal and  $Y$  is one of the IMF components; their variance is:

$$\begin{aligned} D(X) &= E(X^2) - [E(X)]^2 \\ D(Y) &= E(Y^2) - [E(Y)]^2. \end{aligned} \tag{20}$$

The  $BD$  for the variances  $DX$  and  $DY$  are defined as:

$$BD(D(X), D(Y)) = -\ln[BC(D(X), D(Y))]. \quad (21)$$

Here,  $BC$  is the Bhattacharyya coefficient, expressed as:

$$BC(D(X), D(Y)) = \sum_{x \in X, y \in Y} \sqrt{D(x)D(y)}. \quad (22)$$

The relevant IMFs can be determined by evaluating the maximum slope between the  $BD$  of two adjacent IMFs and the original signal. The slope  $\theta$  can be defined as:

$$\theta = \max |BD(n+1) - BD(n)|, n = 1, 2, \dots, (K-1). \quad (23)$$

The demarcation point between the relevant and irrelevant IMFs is  $K_c$ , and the first  $n$  IMFs are selected as the relevant modes in the VMD decomposition.

### 3.4. The Procedure for the WOA-VMD-BD Method

Figure 1 shows the entire procedure for the proposed method. The procedure for the WOA-VMD-BD method is expressed as follows.

- Step 1: Input the signal  $f(t)$ . Initialize the parameters of the WOA, and set the ranges of parameters  $[K, \alpha]$  within the VMD method.
- Step 2: Perform VMD on the signal and compute the fitness value corresponding to each whale according to the Equation (19). The optimal whale position  $\vec{X}^*$  is updated according to the value of  $\vec{A}$  and  $p$ , and the current optimal fitness value and corresponding parameter combination are retained.
- Step 3: Execute step 2 if the calculation satisfies the termination condition; otherwise, repeat step 2 and increase the current number of iterations by 1.
- Step 4: Use the obtained optimal parameters  $[K, \alpha]$  to perform VMD on the signal.
- Step 5: Calculate the  $BD$  between the original signal and each IMF according to Equation (21).
- Step 6: Select the first  $n$  relevant IMFs to reconstruct the signal and output.

Assuming that the signal length is  $N$ , WOA searches two parameters, and the computational complexity of a single WOA is  $O(2N)$ . The computational complexity of VMD is  $O(2N \log_2(2N))$ . VMD is performed once per iteration of WOA. Assuming that the number of iterations is  $MI$ , the computational complexity is  $MI * (O(2N) + O(2N \log_2(2N)))$ . The computational complexity of signal reconstruction using improved Bhattacharyya distance is  $O(N)$ , so the computational complexity of the proposed method is  $MI * (O(2N) + O(2N \log_2(2N))) + O(N)$ .

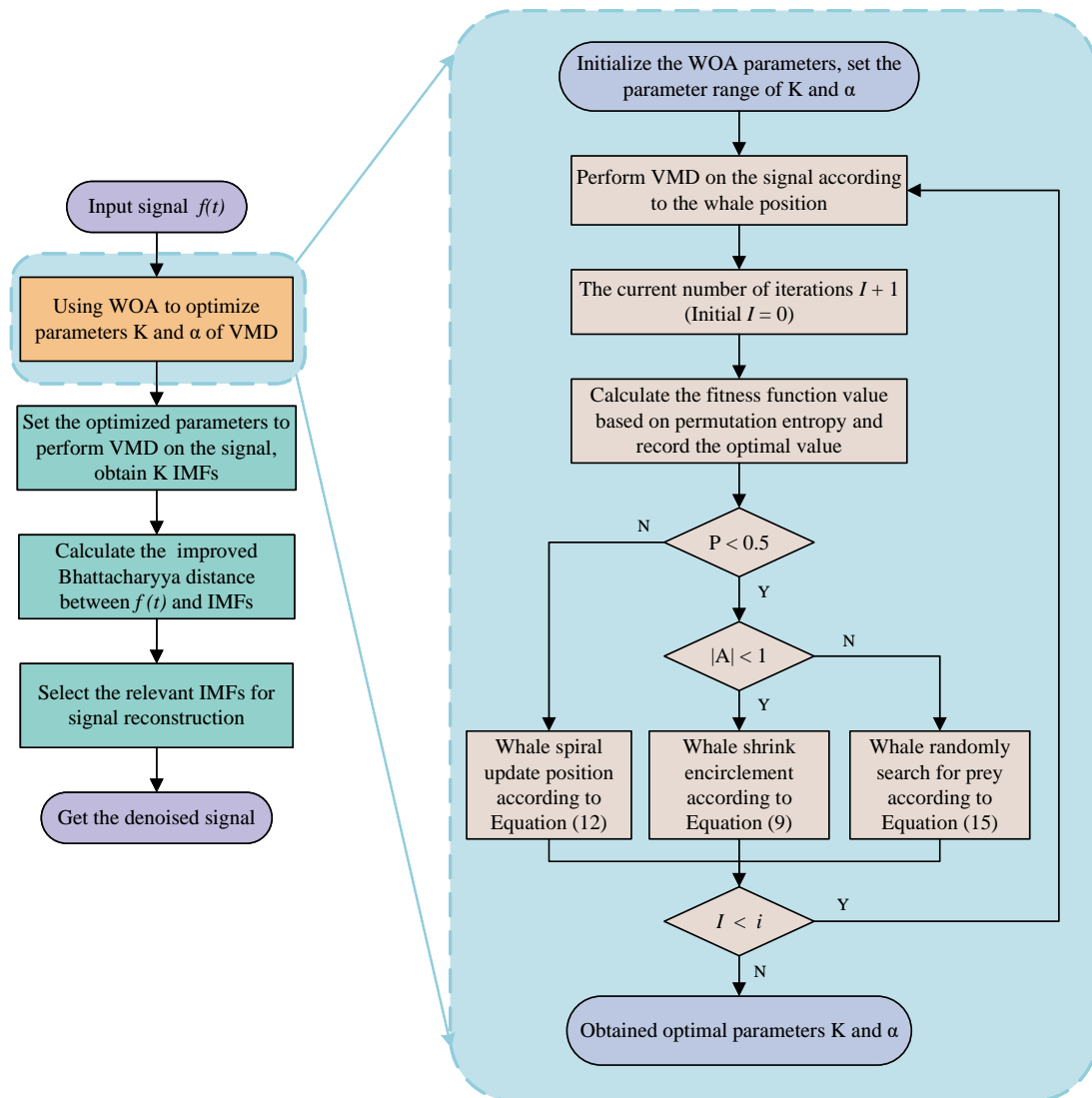


Figure 1. Flow chart of signal denoising method based on WOA-VMD-BD.

#### 4. Simulation

This section evaluates the noise reduction effect of the WOA-VMD-BD method through simulation experiments. We processed the mixed signals and ice-penetrating signals obtained by the three-dimensional structure forward modeling through the WOA-VMD-BD method. To demonstrate the superiority of this method, on the one hand, we set several different  $[K, \alpha]$  combinations to conduct experiments on mixed signals, and the results indicate that the performance of the VMD method is directly influenced by the selection of parameters. On the other hand, comparing the WOA-VMD-BD with the EMD, the results demonstrate that the performance of the WOA-VMD-BD method is significantly better than that of the EMD method.

##### 4.1. Experiment for Mixed Signal

To preliminarily verify the performance of the WOA-VMD-BD method, we used the method to decompose the signal mixed with different frequencies. The mixed signal is composed of four different basic signals. The expression of basic signal 1 is  $\sin(200\pi t)$ , the expression of basic signal 2 is  $0.8\sin(400\pi t)$ , and the expression of basic signal 3 is  $0.5\cos(700\pi t)$ . Basic signal 4 is random noise with amplitude  $A < 0.2$ . The mixed signal and its components are shown in Figure 2.

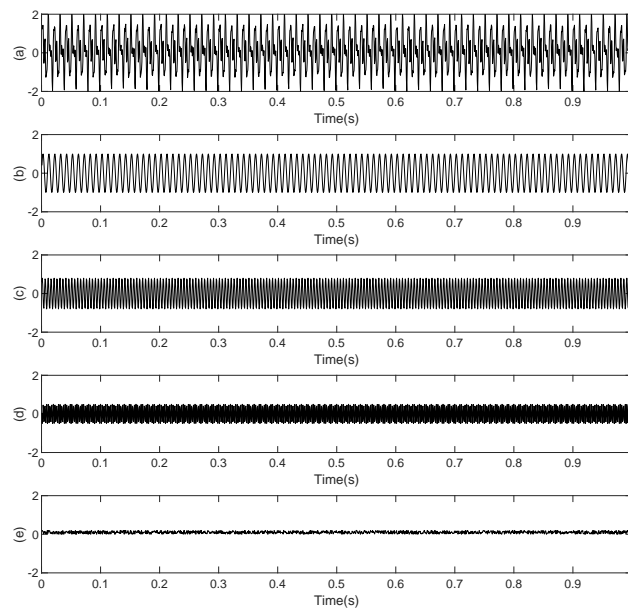


**Figure 2.** The mixed signal and its components. (a) Mixed signal; (b–e) basic signal 1–4.

Set  $[K, \alpha] = [4, 1000]$ , and use the VMD method to decompose the mixed signal. The results are shown in Figure 3. The four components obtained through decomposition can be associated with the basic signals 1 to 4 that constitute the mixed signal, and their waveforms show a high level of consistency. The IMF1 component decomposed from the mixed signal is signal 1, the IMF2 component is signal 3, the IMF3 component is signal 2, and the IMF4 component is signal 4. However, the higher the signal frequency, the more pronounced the envelope of IMF is affected by noise, such as IMF2. It indicates that the noise is not entirely separated from the mixed signal, which is not conducive to displaying ice layer details. The noise interference can be reduced by changing the quadratic penalty factor  $\alpha$ .

In addition, the radar receives different echo signals in detecting the glacier, including the reflection of objects on the ground, the reflection of the ice surface, the reflection of the interface of the inner ice layer, etc. The number of modes  $K$  cannot be determined directly. The decomposition may be incomplete when  $K$  is less than the number of basic signals. For example, set the parameters  $[K, \alpha] = [2, 1000]$ , and again use the VMD method to decompose the mixed signal, and the result is shown in Figure 4. The result shows that the change in the  $K$  value will directly affect the decomposition accuracy, and an inappropriate  $K$  value will reduce the performance of the VMD method.

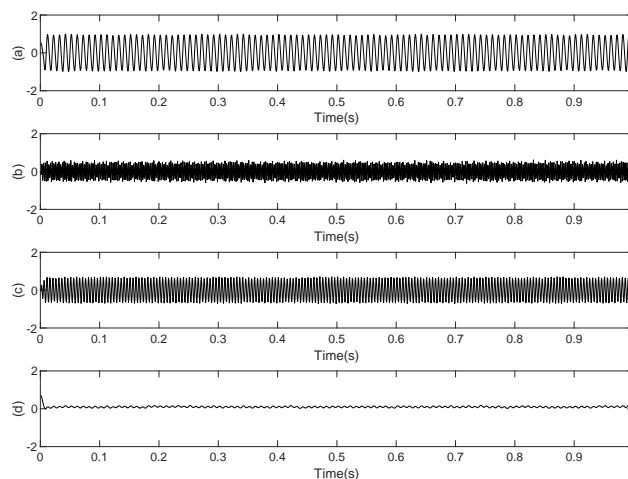


**Figure 3.** The IMF components 1–4 (a–d) of the mixed signal after VMD when  $[K, \alpha] = [4, 1000]$ .

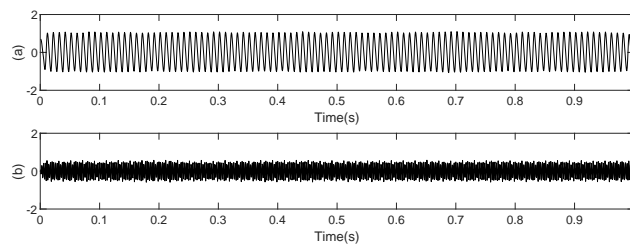


**Figure 4.** The IMF components 1–2 (a,b) of the mixed signal after VMD when  $[K, \alpha] = [2, 1000]$ .

The parameters  $[K, \alpha]$  in the VMD method are optimized by using the WOA. The mixed signal is decomposed by VMD using the optimized parameters. The decomposition results are shown in Figure 5. After 15 iterations, the optimal parameters were obtained, and  $[K, \alpha] = [4, 3319]$  was set. The corresponding relationship after decomposition is: IMF1–4 correspond to signals 1–4, respectively. The IMFs is less affected by noise, and the performance of VMD is improved.

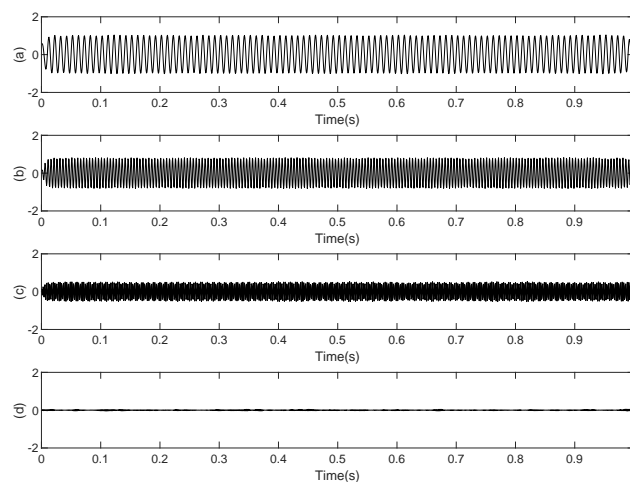


**Figure 5.** The IMF components 1–4 (a–d) of the mixed signal after VMD when  $[K, \alpha] = [4, 3319]$ .

In order to indicate the decomposition ability of the WOA-VMD-BD, this paper selects the EMD method and WOA-VMD-BD method for comparison. The four IMFs after EMD decomposition of the mixed signal are shown in Figure 6, and the corresponding relationship with the basic signal is: the IMF1 component decomposed from the mixed signal is signal 3, the IMF2 component is signal 2, the IMF3 component is signal 1, and the IMF4 component is signal 4. It can be seen from the figure that there are many abrupt peaks in the four IMF components at this time, which affects the corresponding relationship with the four basic signals. From the decomposition results, it can be seen that the decomposition performance of EMD is inferior to that of WOA-VMD-BD.

The SNR of the mixed signal after decomposition and recombination evaluates the noise reduction performance. The improved BD between the mixed signal and the IMFs decomposed by the VMD method, WOA-VMD-BD method, and EMD method (corresponding to Figure 3, Figure 5, and Figure 6, respectively) is calculated. When manually setting parameters  $[K, \alpha] = [4, 1000]$  at random for VMD, the BD between the 4 IMFs and the mixed signal are  $[0.43, 1.25, 0.78, 2.92]$ . After optimization by the WOA, set the parameters  $[K, \alpha] = [4, 3319]$  when VMD is performed, the BD is  $[0.37, 0.60, 1.06, 4.15]$ . The BD of the four IMFs after EMD and the mixed signal is  $[0.89, 0.66, 0.42, 2.23]$ . Figure 7 shows the line diagram of the BD. The abscissa IMF $_k$  in the figure represents the serial number of the IMF. According to Equation (23), the maximum slope of the two adjacent BD was selected as the demarcation point, and the first three IMFs were selected for signal recombination.

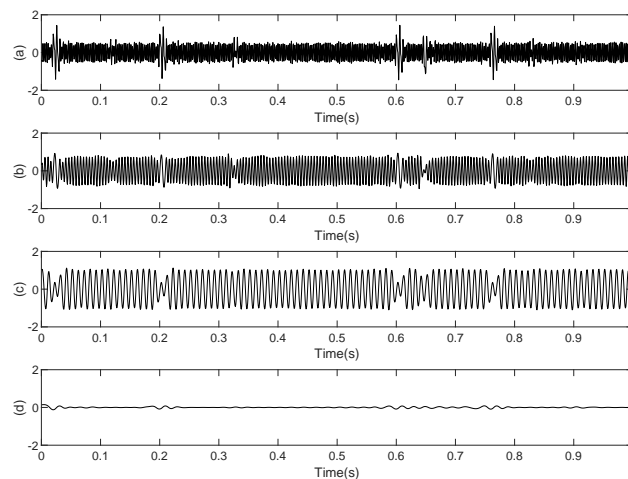


**Figure 6.** The IMF components 1–4 (a–d) of the mixed signal after EMD.

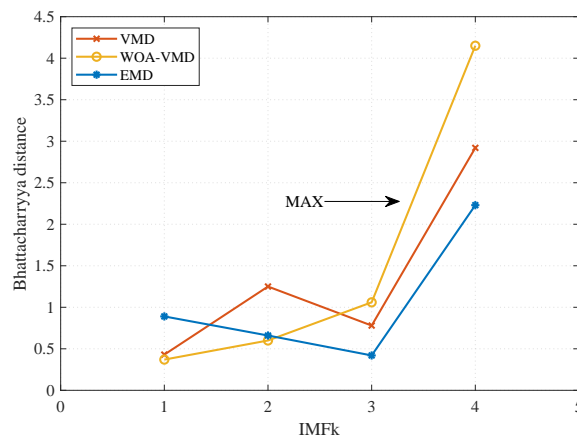


**Figure 7.** Improved Bhattacharyya distance between IMFs and mixed signal.

The SNR of the mixed signal is 18.56 dB. After processing by the VMD method, WOA-VMD-BD method, and EMD method, the SNR of the recombined signal is 22.46 dB, 24.63 dB, and 21.39 dB, respectively. The denoising effect of the WOA-VMD-BD method is more accurate than the other two methods. The WOA-VMD-BD method can overcome the limitations of the VMD method and the EMD method and enhance the noise reduction performance of the VMD method to a certain extent.

#### 4.2. Simulation of the 3D Structure Model

To further verify the effectiveness of the WOA-VMD-BD method for denoising the ice penetration signal, this section uses the method to process the simulated ice-penetrating signals. We established a three-dimensional ice structure model and employed the three-dimensional finite difference time domain (FDTD) method to perform forward modeling on the model to obtain simulated ice-penetrating signals. The specific principle of FDTD can refer to [29,30]. Finally, we used the WOA-VMD-BD method to decompose and reconstruct the data, and the results were analyzed.

In this paper, a three-dimensional model with a size of 8 m × 16 m × 2 m was constructed, as shown in Figure 8. The model consists of an air layer and three ice layers. The thickness of the air layer is 2 m. The first layer interface represents the interface between the air and the ice layer 1, the ice surface where the radar survey line is located, at a depth of 0 m. The second layer interface represents the interface between ice layer 1 and ice layer 2, located at a depth of 5 m. The third layer interface represents the interface between ice layer 2 and ice layer 3, which is located at a depth of 9 m. In order to be closer to the actual situation, the interfaces between the ice layers were designed as rough interfaces

with slight fluctuations. The relative permittivity of the three ice layers are 2.98, 3.05, and 3.16, respectively. The specific parameters are shown in Table 1.

**Table 1.** The 3D ice structure model parameters.

Composition	Depth (m)	Relative Permittivity $\epsilon_r$	Conductivity $\sigma$ (S/m)
Air	−2–0	1	0
Ice layer 1	0–5	2.98	0.0001
Ice layer 2	5–9	3.05	0.0002
Ice layer 3	9–14	3.16	0.0004

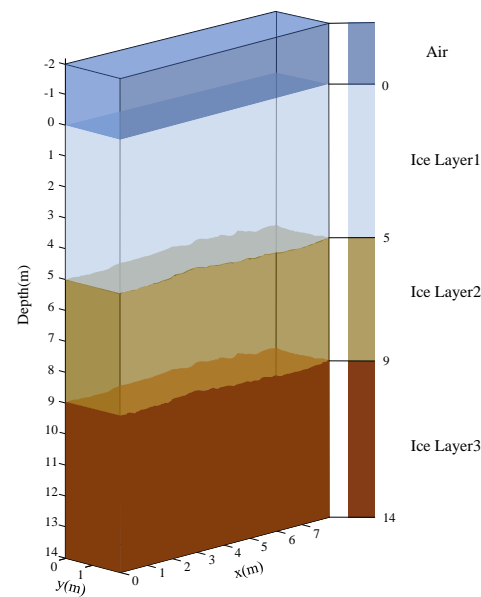


**Figure 8.** The 3D ice structure model.

The center frequency of the simulated antenna is set to 500 MHz. The distance between the transmitting and receiving antennas is 0.1 m, and the antenna is located 0.3 m above the interface between the air and the glacier. The offset of the antenna is 0.04 m. The sampling frequency is 2.6 GHz. The time window of acquisition is 160 ns, and 150 channels of data are collected. Since the pseudo-random coded radar we used can collect data in HH polarization and HV polarization modes, the simulation experiment also collected data in two polarization modes. After preprocessing, such as direct wave removal, zero-point correction, and gain, the simulated glacier profiles collected in HH and HV polarization modes are shown in Figure 9. The 75th track of the two profiles is shown in Figure 10.

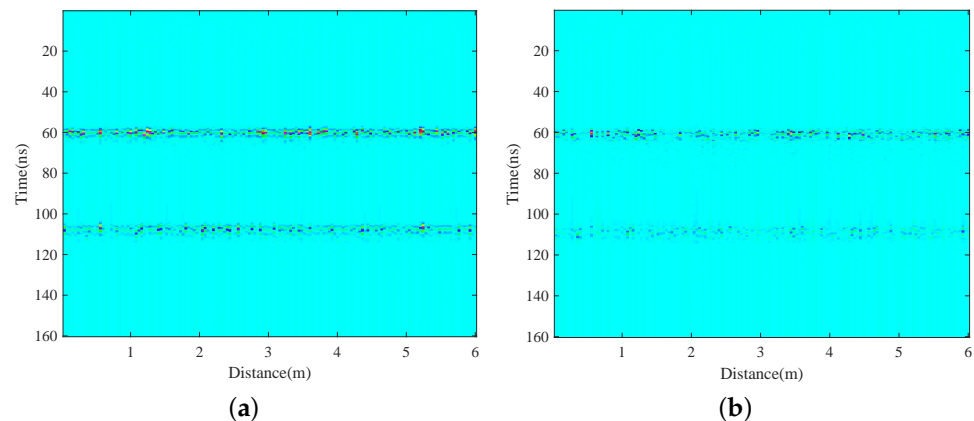


**Figure 9.** The simulated profiles. (a) HH polarization mode. (b) HV polarization mode.

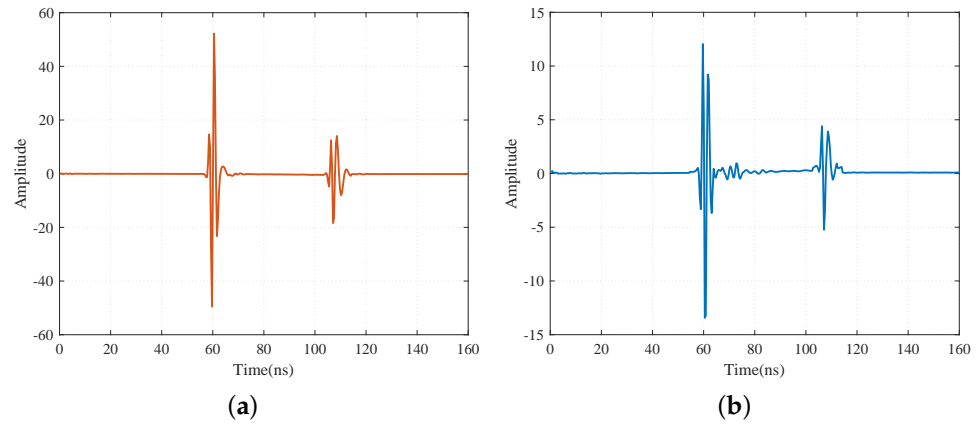


**Figure 10.** The 75th trace of profiles. (a) HH polarization mode. (b) HV polarization mode.

Add 10 dBw Gaussian noise to the simulated data, then decompose and reconstruct it using the WOA-VMD-BD method. After adding noise, the layered interface details are covered. The simulated profiles in HH and HV polarization modes and the corresponding data of the 75th track are shown in Figures 11 and 12.

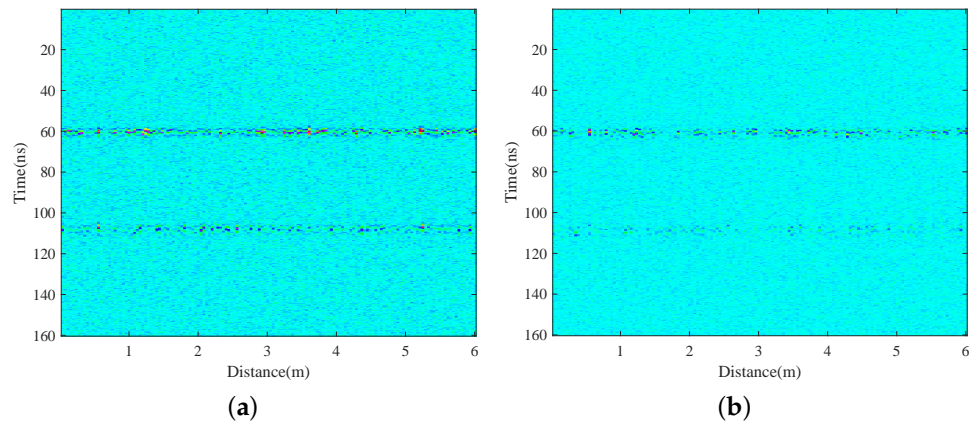


**Figure 11.** Simulated profiles after adding noise. (a) HH polarization mode. (b) HV polarization mode.

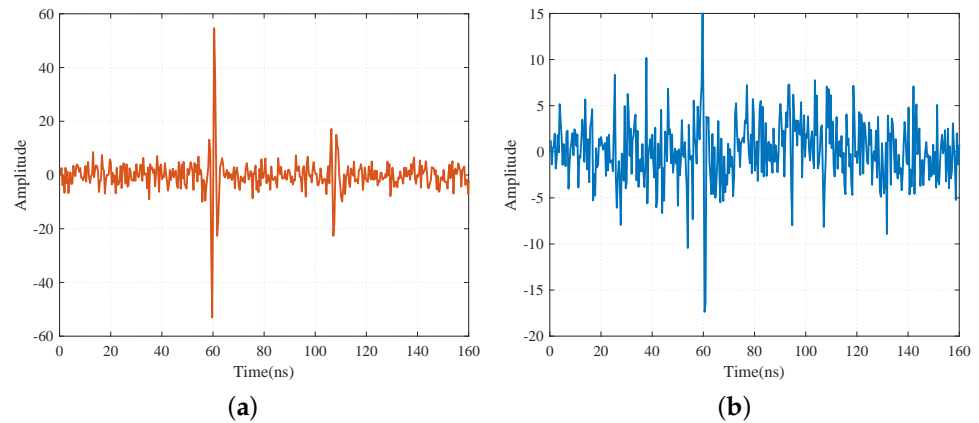


**Figure 12.** The 75th trace of profiles after adding noise. (a) HH polarization mode. (b) HV polarization mode.

The WOA-VMD-BD method was employed to process the data above. The WOA searches for the parameters  $[K, \alpha]$  of the VMD. The initial value of the parameter combination  $[K, \alpha]$  was set between  $[1000-9000, 3-9]$ , with 10 WOA search agents and 30 iterations.

The permutation entropy (PE) was used to calculate the fitness value of WOA to optimize the parameters of the VMD method iteratively. The fitness value convergence curves of the iterative update in HH and HV polarization modes are shown in Figure 13. The fitness values converge in the 12th and 5th iterations, respectively, and the minimum fitness value is 0.76 and 0.81.

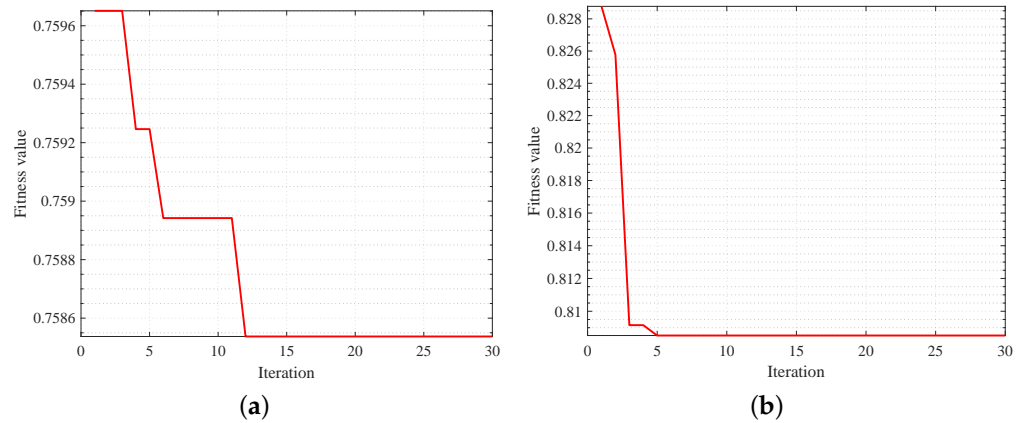


**Figure 13.** Convergence curve of WOA-VMD-BD fitness function of simulated data. (a) HH polarization mode. (b) HV polarization mode.

The optimal parameters  $[K, \alpha]$  searched by WOA in HH and HV polarization modes are  $[4, 2068]$  and  $[4, 1281]$ , respectively. Figures 14 and 15 show the IMF components obtained after VMD processing based on parameters optimized by WOA. According to the information in the figures, IMF1 and IMF2 contain more obvious stratification information of glacier. To quantify the valuable information present in each IMF component, we computed the BD between each IMF and the original signal in the two polarization modes:  $[2.98, 3.19, 3.65, 3.71]$  and  $[2.28, 2.40, 2.73, 2.79]$ . The maximum slopes of the two groups of BD appear between IMF2 and IMF3, so the first two IMFs were selected for recombination.

The recombination profiles in HH and HV polarization modes are shown in Figure 16. Comparing to the noised profiles in Figure 11, the profiles processed by WOA-VMD-BD are more precise, and the stratified interfaces are more detailed than before. Similarly, to demonstrate the strengths of the WOA-VMD-BD method, we compared this method with the EMD method. The profile after EMD processing is shown in Figure 17. The method only removes part of the noise, and the details of the layered interfaces in the glacier are not displayed clearly. We calculated the SNR of the data before and after processing in the two polarization modes, as shown in Table 2. The superiority of the WOA-VMD-BD method was further verified by comparing figures and data. Compared with the EMD method, the WOA-VMD-BD method can mitigate noise more effectively and enhance the signal-to-noise ratio.

**Table 2.** Signal-to-noise ratio of data before and after processing.

Polarization Mode	Algorithms		
	Raw Data	WOA-VMD-BD	EMD
HH	27.3dB	35.9 dB	30.3 dB
HV	21.0 dB	30.8 dB	24.8 dB

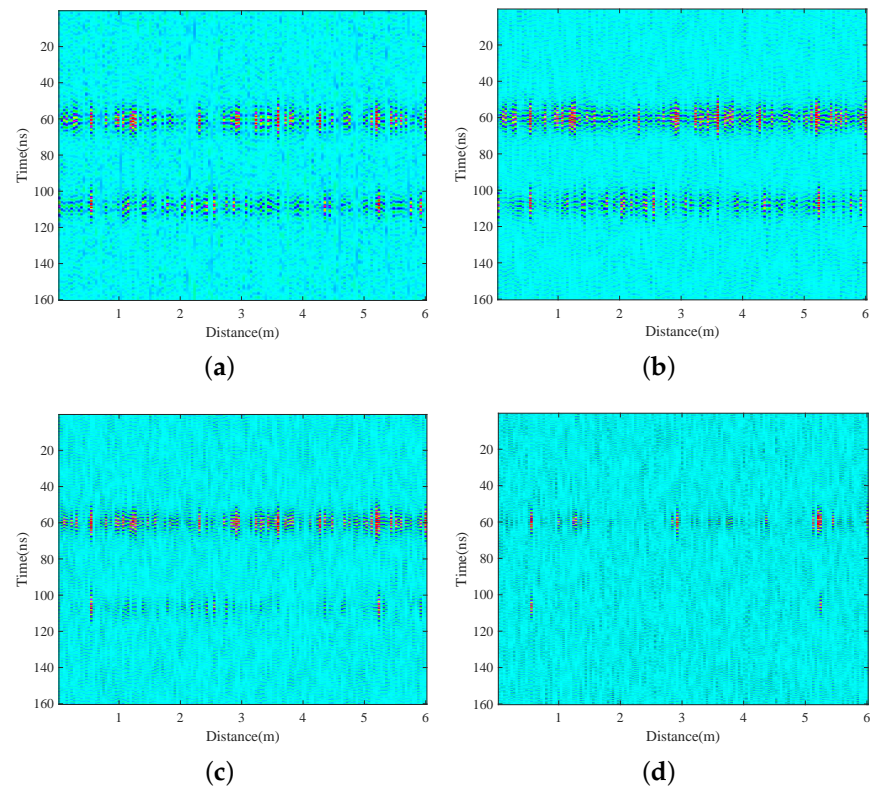


**Figure 14.** The IMFs obtained by WOA-VMD-BD of the simulated data in HH polarization mode. (a) IMF1. (b) IMF2. (c) IMF3. (d) IMF4.

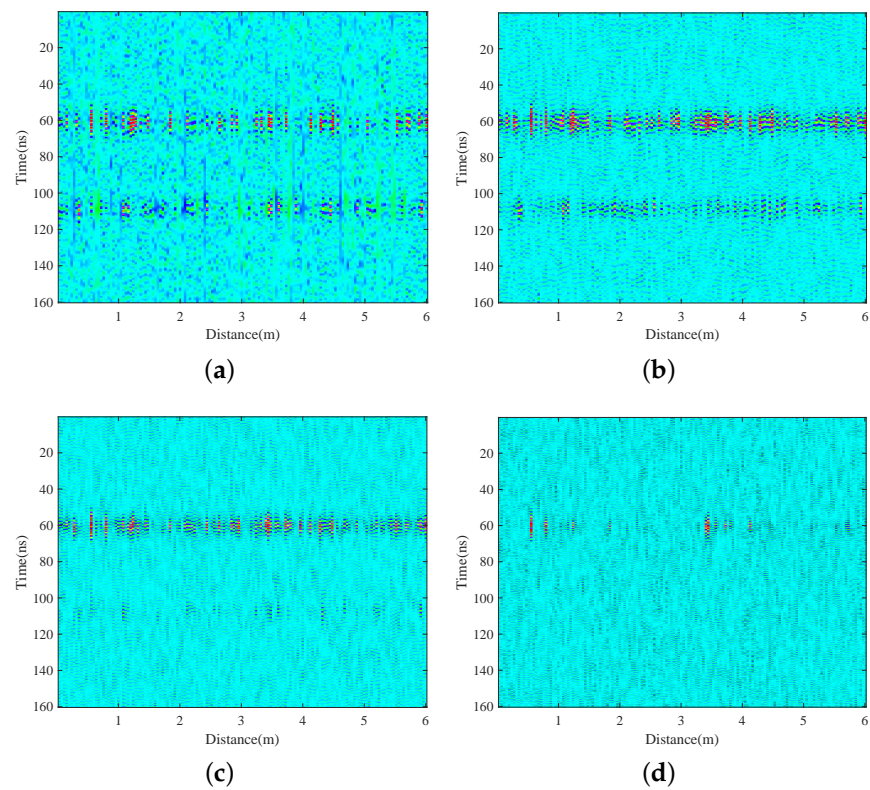


**Figure 15.** The IMFs obtained by WOA-VMD-BD of the simulated data in HV polarization mode. (a) IMF1. (b) IMF2. (c) IMF3. (d) IMF4.

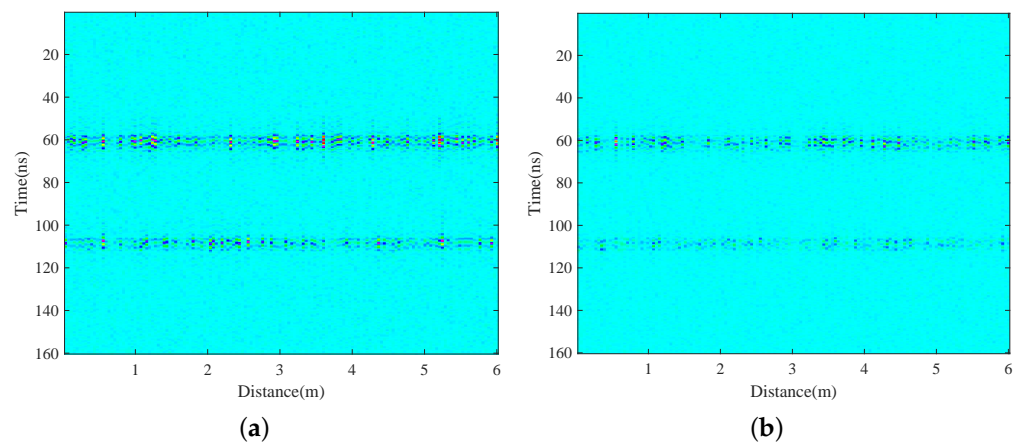


**Figure 16.** Simulated profiles of IMF1 and IMF2 combined after WOA-VMD-BD processing. (a) HH polarization mode. (b) HV polarization mode.

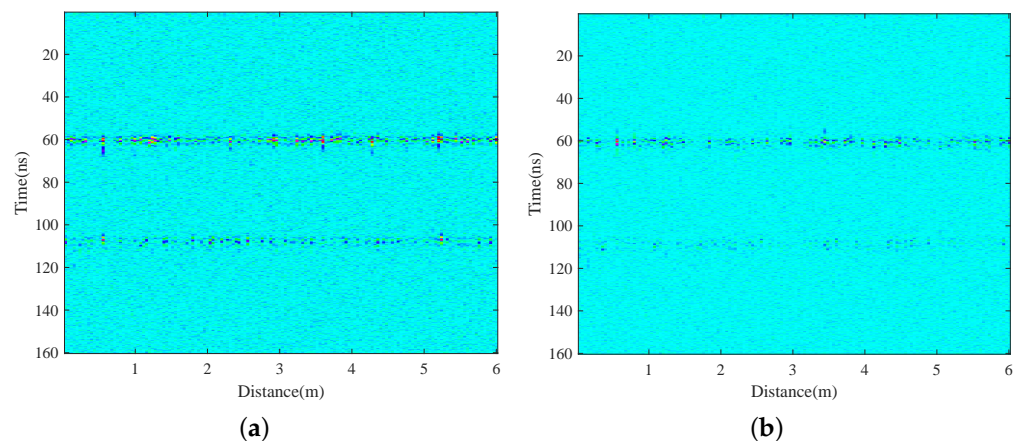


**Figure 17.** Simulated profiles after EMD processing. (a) HH polarization mode. (b) HV polarization mode.

## 5. Field Measurement and Verification Results

To better meet the needs of scientific exploration data applications and research, the laboratory staff conducted a verification experiment at the Mengke No. 29 Glacier in September 2022. The Mengke No. 29 Glacier is located in Gansu Province, China, with an area of 7.1 square kilometers and a length of 6.5 km. It is the largest glacier in the Danghenan Mountains. The current height of the exposed ice is about 4350 m above sea level, and the height of the top of the glacier exceeds 5100 m. The upper part of the glacier tongue is crisscrossed with cracks. Therefore, Mengke Glacier No. 29 provides an excellent ground verification test condition for exploring the lunar regolith layer structure.

The experiment used a laboratory-built pseudo-random-coded UWB radar. The radar comprises electronic units, high-frequency channel transmitters, low-frequency channel transmitters, low-frequency channel antennas, high-frequency channel antennas, and cables. The schematic diagram of the radar device is shown in Figure 18.

Figure 19 shows the on-site detection scene. The high-frequency channel antennas are installed at the bottom of the trolley, the low-frequency channel antennas are installed on both sides of the top plate of the trolley, and the electronic unit is installed inside the trolley. A host computer program controls the radar. The echo data received by the high-frequency channel was used in this experiment. The high-frequency channel uses 128 bit code elements, and the center frequency of the code element signal is 800 MHz, with a transmission signal frequency range covering 100–1400 MHz. The transmission power is 0.4 W, the reception window is 2.16 ns, the mixed sampling rate is 5.12 GHz,

and the reception gain is 50 dB. The Botiew antenna is located 0.3 m above the ground, providing good antenna coupling and detection quality. The survey line length is 1 m, and the antenna offset is 0.001 m. The images of the collected data in HH and HV polarization modes after pre-processing, such as DC removal, gain, and zero-point correction, are shown in Figure 20.

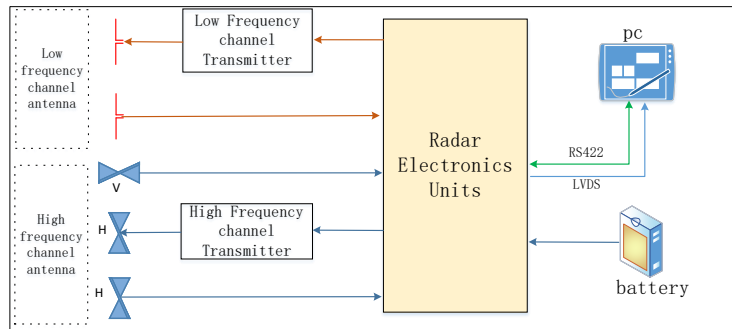


Figure 18. The schematic diagram of the radar device.



Figure 19. Field experiments were carried out on the Glacier Mengke 29. (A) is the high-frequency channel antennas, (B) is the low-frequency channel antennas, and (C) is the electronic unit.

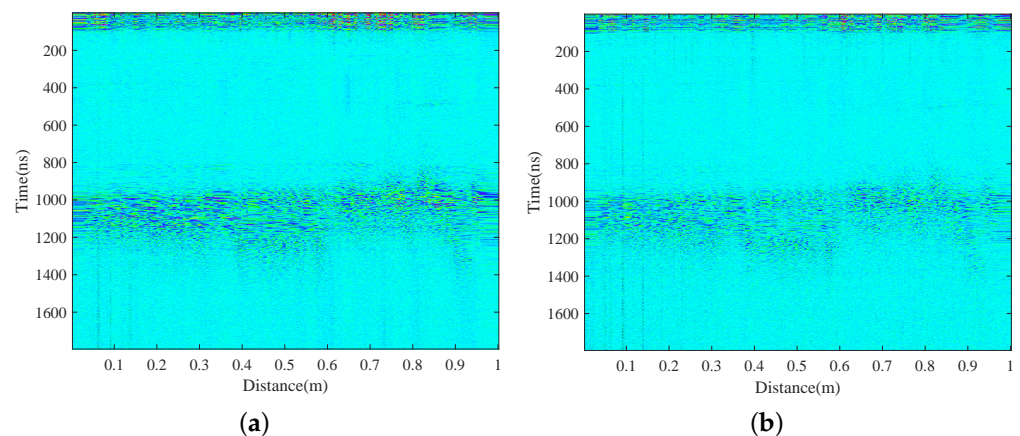
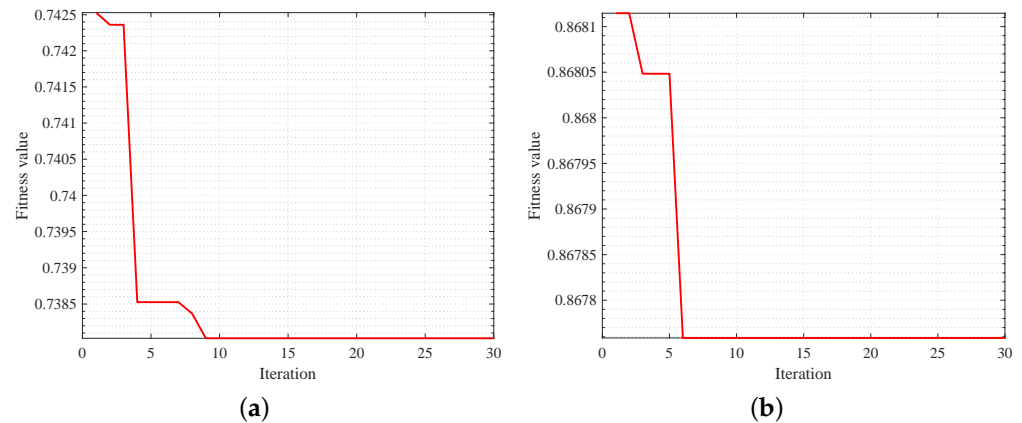


Figure 20. Glacier profiles after pre-processing. (a) HH polarization mode. (b) HV polarization mode.

The position of ordinate 0–80 ns is the interface between the air and ice glacier. The information shown in the above two figures shows that a layered interface inside the glacier appears at the position of the ordinate 1000–1200 ns. Among them, compared with the signal collected in the HV polarization mode, the signal collected in the HH polarization mode has stronger energy and more obvious stratification characteristics. There is still

some interference noise in the data after simple processing, which affects our judgment and description of the details of the layered interface. Therefore, we used the WOA-VMD-BD method to process the data set further. Figure 21 shows the convergence curves of WOA-VMD-BD parameter optimization for the data acquired in two polarization modes. The WOA-VMD-BD fitness function converges at the 9th and 6th iterations, and the minimum fitness values are 0.74 and 0.87.



**Figure 21.** Convergence curve of fitness function of WOA-VMD-BD of measured data. (a) HH polarization mode. (b) HV polarization mode.

The optimal values of parameters  $[K, \alpha]$  for HH and HV polarization modes, obtained using WOA, are rounded to  $[4, 3226]$  and  $[4, 3103]$ , respectively, which are used as the input parameters for the VMD method. The acquired datasets from the two polarization modes were decomposed into IMFs using the corresponding optimal parameters, as shown in Figures 22 and 23. Regardless of the data acquired by any polarization mode, IMF1 to IMF3 contain the primary reflection information of the layered interface in the glacier, while IMF4 mainly contains noise components. The calculated BD for the two groups are  $[10.13, 10.47, 10.30, 9.18]$  and  $[10.02, 10.29, 10.11, 9.63]$ , respectively, and their maximum slope appears between IMF3 and IMF4 also prove this information.

Figure 24 shows the reconstructed profiles of the first three IMFs. Compared to Figure 19, the clarity has been notably enhanced. The layered interface in the glacier, especially the situation below the layered interface, can be observed more clearly. The evaluation criterion of image entropy [31,32] is introduced, representing the degree of chaos in an image. The larger the image entropy, the more affected the image is by noise, and the more difficult it is to extract layered information in the glacier; the smaller the image entropy, the more conducive it is to target recognition. After calculations, the image entropy of the original profile obtained by HH and HV polarization modes was 5072.4 and 5359.2, and the image entropy after WOA-VMD-BD processing was 4545.5 and 4822.3. The WOA-VMD-BD method effectively reduces the image entropy of the profile and removes part of the noise. The above experiments further prove the excellent performance of the WOA-VMD-BD method in reducing noise in pseudo-random coded radar data and provide some help in observing lunar regolith profiles and data interpretation in subsequent space exploration missions.

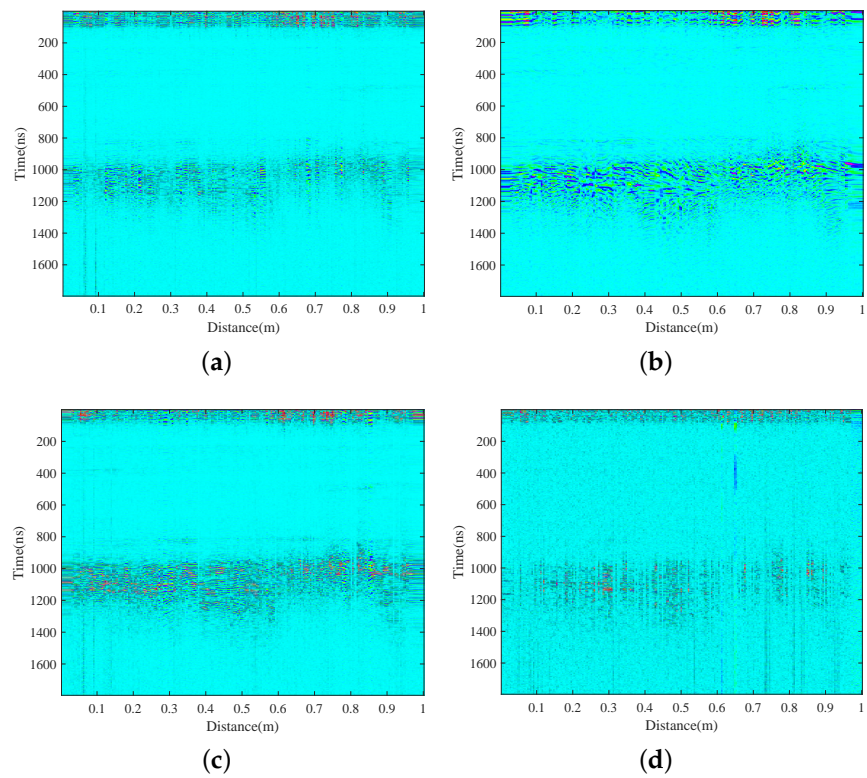


**Figure 22.** The IMFs obtained by WOA-VMD-BD of the measured data in HH polarization mode. (a) IMF1. (b) IMF2. (c) IMF3. (d) IMF4.

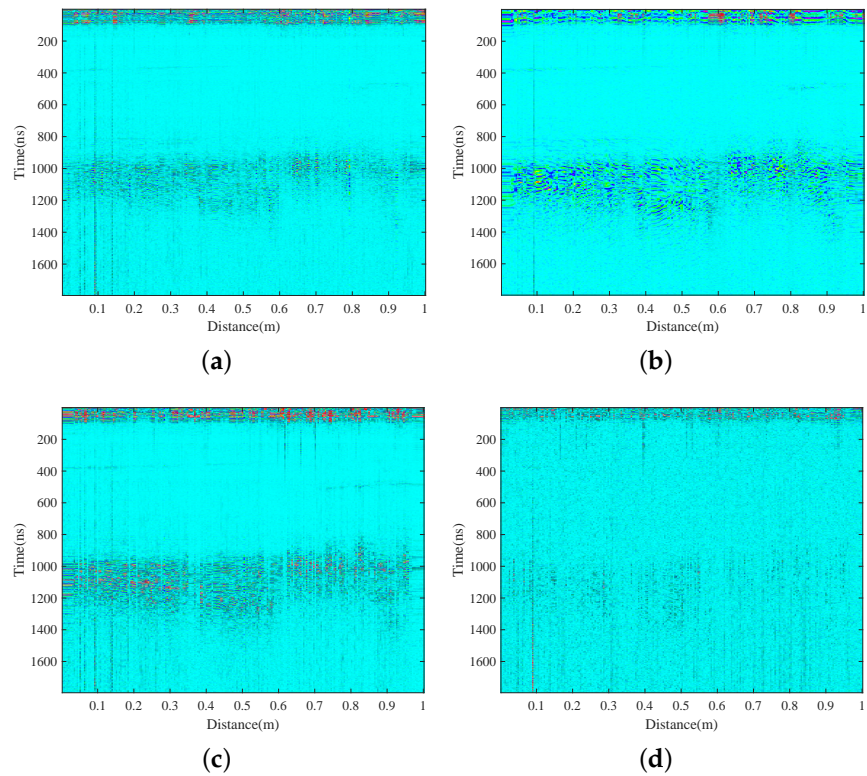


**Figure 23.** The IMFs obtained by WOA-VMD-BD of the measured data in HV polarization mode. (a) IMF1. (b) IMF2. (c) IMF3. (d) IMF4.

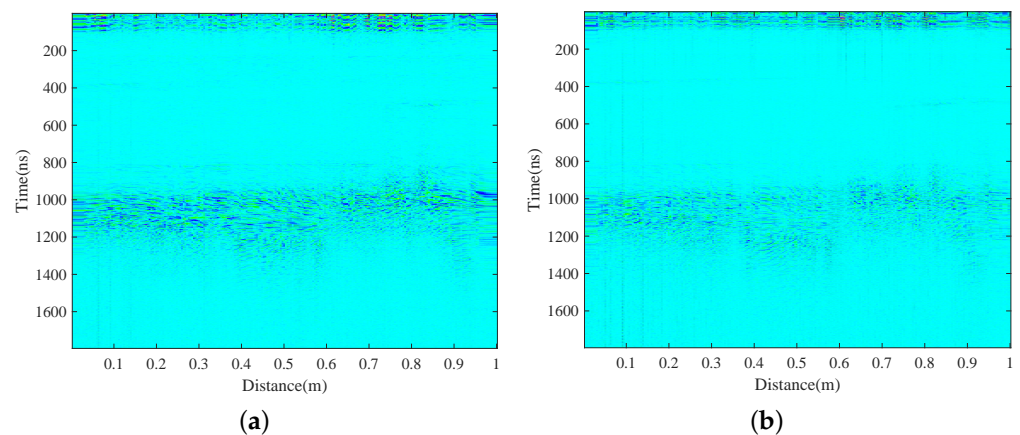


**Figure 24.** Glacier profiles of IMF1 and IMF2 combined after WOA-VMD-BD processing. (a) HH polarization mode. (b) HV polarization mode.

## 6. Conclusions

This paper proposes applying the WOA-VMD-BD method to ice-penetrating signal denoising. The proposed method combines VMD's powerful signal decomposition ability and the parameter search ability of WOA based on permutation entropy. Following that, it measures the similarity of signals according to the BD to achieve an efficient and accurate denoising effect. Experimental results on mixed signals show that the selection of parameters  $K$  and  $\alpha$  directly impact the performance of the VMD method. In addition, we also perform forward modeling on the three-dimensional ice layer structure model. The results show that the WOA-VMD-BD method has better anti-noise ability than EMD and can effectively improve the SNR of the signal. In the experiment of measured data of the glacier, the WOA-VMD-BD method effectively reduced the noise in the ice profiles. The details of the glacier's layered interface are more precise than those of the original profiles. The method can improve the quality of ice-penetrating signals and help to reveal the details of the ice-layered structure. The denoising method is expected to be applied in space exploration. If a proper WOA fitness function is established in combination with signal characteristics, this method also has exploration value in other signal processing fields.

**Author Contributions:** Theory analysis, D.L., S.S. and Y.L.; Data acquisition, D.L. and S.S.; Methodology, D.L.; Project administration, S.S., X.L. and G.F.; Software, D.L.; Validation, D.L. and B.Z.; Visualization, D.L.; Writing manuscript, D.L. All authors have read and agreed to the published version of the manuscript.

**Funding:** This work was funded by Research on Key Technology of Ice Crack Detection Radar, National Key Research and Development Program (2021YFC2801404), National Natural Science Foundation of China (41776204).

**Data Availability Statement:** Not applicable.

**Conflicts of Interest:** The authors have no conflict of interest to disclose.

## References

1. Xia, Z.; Fang, G.; Ye, S.; Zhang, Q.; Chen, C.; Yin, H. A Novel Handheld Pseudo Random Coded UWB Radar for Human Sensing Applications. *IEICE Electron. Express* **2014**, *11*, 20140981. [[CrossRef](#)]
2. Lai, W.L.; Kind, T.; Wiggerhauser, H. A Study of Concrete Hydration and Dielectric Relaxation Mechanism Using Ground Penetrating Radar and Short-Time Fourier Transform. *EURASIP J. Adv. Signal Process.* **2010**, *2010*, 317216. [[CrossRef](#)]
3. Hayashi, N.; Sato, M.  $F - k$  Filter Designs to Suppress Direct Waves for Bistatic Ground Penetrating Radar. *IEEE Trans. Geosci. Remote Sens.* **2010**, *48*, 1433–1444. [[CrossRef](#)]
4. Wong, P.T.W.; Lai, W.W.L.; Sato, M. Time-Frequency Spectral Analysis of Step Frequency Continuous Wave and Impulse Ground Penetrating Radar. In Proceedings of the 2016 16th International Conference on Ground Penetrating Radar (GPR), Hong Kong, China, 13–16 June 2016; pp. 1–6. [[CrossRef](#)]
5. Rehman, N.; Aftab, H. Multivariate Variational Mode Decomposition. *IEEE Trans. Signal Process.* **2019**, *67*, 6039–6052. [[CrossRef](#)]

6. Jiang, L.; Zhou, X.; Che, L.; Rong, S.; Wen, H. Feature Extraction and Reconstruction by Using 2D-VMD Based on Carrier-Free UWB Radar Application in Human Motion Recognition. *Sensors* **2019**, *19*, 1962. [[CrossRef](#)]
7. Huang, N.E.; Shen, Z.; Long, S.R.; Wu, M.C.; Shih, H.H.; Zheng, Q.; Yen, N.C.; Tung, C.C.; Liu, H.H. The empirical mode decomposition and the Hilbert spectrum for nonlinear and non-stationary time series analysis. *Proc. R. Soc. Lond. Ser. A Math. Phys. Eng. Sci.* **1998**, *454*, 903–995. [[CrossRef](#)]
8. Wang, Y.; Markert, R. Filter Bank Property of Variational Mode Decomposition and Its Applications. *Signal Process.* **2016**, *120*, 509–521. [[CrossRef](#)]
9. Gilles, J. Empirical Wavelet Transform. *IEEE Trans. Signal Process.* **2013**, *61*, 3999–4010. [[CrossRef](#)]
10. Huang, N.; Chen, H.; Cai, G.; Fang, L.; Wang, Y. Mechanical Fault Diagnosis of High Voltage Circuit Breakers Based on Variational Mode Decomposition and Multi-Layer Classifier. *Sensors* **2016**, *16*, 1887. [[CrossRef](#)]
11. Dragomiretskiy, K.; Zosso, D. Variational Mode Decomposition. *IEEE Trans. Signal Process.* **2014**, *62*, 531–544. [[CrossRef](#)]
12. Liu, Y.; Yang, G.; Li, M.; Yin, H. Variational Mode Decomposition Denoising Combined the Detrended Fluctuation Analysis. *Signal Process.* **2016**, *125*, 349–364. [[CrossRef](#)]
13. Huang, Y.; Bao, H.; Qi, X. Seismic Random Noise Attenuation Method Based on Variational Mode Decomposition and Correlation Coefficients. *Electronics* **2018**, *7*, 280. [[CrossRef](#)]
14. Xiao, Q.; Li, J.; Zeng, Z. A Denoising Scheme for DSPI Phase Based on Improved Variational Mode Decomposition. *Mech. Syst. Signal Process.* **2018**, *110*, 28–41. [[CrossRef](#)]
15. Li, H.; Chang, J.; Xu, F.; Liu, Z.; Yang, Z.; Zhang, L.; Zhang, S.; Mao, R.; Dou, X.; Liu, B. Efficient Lidar Signal Denoising Algorithm Using Variational Mode Decomposition Combined with a Whale Optimization Algorithm. *Remote Sens.* **2019**, *11*, 126. [[CrossRef](#)]
16. Lu, J.; Yue, J.; Zhu, L.; Wang, D.; Li, G. An Improved Variational Mode Decomposition Method Based on the Optimization of Salp Swarm Algorithm Used for Denoising of Natural Gas Pipeline Leakage Signal. *Measurement* **2021**, *185*, 110107. [[CrossRef](#)]
17. Huang, Y.; Yan, L.; Cheng, Y.; Qi, X.; Li, Z. Coal Thickness Prediction Method Based on VMD and LSTM. *Electronics* **2022**, *11*, 232. [[CrossRef](#)]
18. Liu, S.; Chen, Y.; Luo, C.; Jiang, H.; Li, H.; Li, H.; Lu, Q. Particle Swarm Optimization-Based Variational Mode Decomposition for Ground Penetrating Radar Data Denoising. *Remote Sens.* **2022**, *14*, 2973. [[CrossRef](#)]
19. Cheng, S.; Liu, S.; Guo, J.; Luo, K.; Zhang, L.; Tang, X. Data Processing and Interpretation of Antarctic Ice-Penetrating Radar Based on Variational Mode Decomposition. *Remote Sens.* **2019**, *11*, 1253. [[CrossRef](#)]
20. Wei, D.; Jiang, H.; Shao, H.; Li, X.; Lin, Y. An Optimal Variational Mode Decomposition for Rolling Bearing Fault Feature Extraction. *Meas. Sci. Technol.* **2019**, *30*, 055004. [[CrossRef](#)]
21. Mirjalili, S.; Lewis, A. The Whale Optimization Algorithm. *Adv. Eng. Softw.* **2016**, *95*, 51–67. [[CrossRef](#)]
22. Lu, J.; Yue, J.; Zhu, L.; Li, G. Variational Mode Decomposition Denoising Combined with Improved Bhattacharyya Distance. *Measurement* **2020**, *151*, 107283. [[CrossRef](#)]
23. Qi, Q.; Zhao, Y.; Zhang, L.; Yang, Z.; Sun, L.; Jia, X. Research on Ultra-Wideband Radar Echo Signal Processing Method Based on P-Order Extraction and VMD. *Sensors* **2022**, *22*, 6726. [[CrossRef](#)][[PubMed](#)]
24. Liu, N.; Li, F.; Wang, D.; Gao, J.; Xu, Z. Ground-Roll Separation and Attenuation Using Curvelet-Based Multichannel Variational Mode Decomposition. *IEEE Trans. Geosci. Remote Sens.* **2022**, *60*, 5901214. [[CrossRef](#)]
25. Yan, H.; Xu, T.; Wang, P.; Zhang, L.; Hu, H.; Bai, Y. MEMS Hydrophone Signal Denoising and Baseline Drift Removal Algorithm Based on Parameter-Optimized Variational Mode Decomposition and Correlation Coefficient. *Sensors* **2019**, *19*, 4622. [[CrossRef](#)]
26. Feng, G.; Wei, H.; Qi, T.; Pei, X.; Wang, H. A Transient Electromagnetic Signal Denoising Method Based on an Improved Variational Mode Decomposition Algorithm. *Measurement* **2021**, *184*, 109815. [[CrossRef](#)]
27. Zhong, J.; Gou, X.; Shu, Q.; Liu, X.; Zeng, Q. A FOD Detection Approach on Millimeter-Wave Radar Sensors Based on Optimal VMD and SVDD. *Sensors* **2021**, *21*, 997. [[CrossRef](#)]
28. Chen, Q.Q.; Dai, S.W.; Dai, H.D. A Rolling Bearing Fault Diagnosis Method Based on EMD and Quantile Permutation Entropy. *Math. Probl. Eng.* **2019**, *2019*, e3089417. [[CrossRef](#)]
29. Gurel, L.; Oguz, U. Three-Dimensional FDTD Modeling of a Ground-Penetrating Radar. *IEEE Trans. Geosci. Remote Sens.* **2000**, *38*, 1513–1521. [[CrossRef](#)]
30. Lee, K.H.; Chen, C.C.; Teixeira, F.; Lee, R. Modeling and Investigation of a Geometrically Complex UWB GPR Antenna Using FDTD. *IEEE Trans. Antennas Propag.* **2004**, *52*, 1983–1991. [[CrossRef](#)]
31. Xu, X.; Miller, E. Entropy Optimized Contrast Stretch to Enhance Remote Sensing Imagery. In Proceedings of the 2002 International Conference on Pattern Recognition, Quebec City, QC, Canada, 11–15 August 2002; Volume 3, pp. 915–918. [[CrossRef](#)]
32. Wang, Y.; Feng, X.; Zhou, H.; Dong, Z.; Liang, W.; Xue, C.; Li, X. Water Ice Detection Research in Utopia Planitia Based on Simulation of Mars Rover Full-Polarimetric Subsurface Penetrating Radar. *Remote Sens.* **2021**, *13*, 2685. [[CrossRef](#)]

**Disclaimer/Publisher's Note:** The statements, opinions and data contained in all publications are solely those of the individual author(s) and contributor(s) and not of MDPI and/or the editor(s). MDPI and/or the editor(s) disclaim responsibility for any injury to people or property resulting from any ideas, methods, instructions or products referred to in the content.